Supporting information

Designing SnS/MoS_2 van der Waals heterojunction for direct Z-scheme photocatalytic overall water-splitting by DFT investigation

Xiaofang Jia, [a] Jinlong Wang,[b] Yue Lu,[a] Jiaming Sun,[a] Yang Li,[a] Yuyan Wang*[c] and Junying Zhang*[a]

[a] *School of Physics, Beihang University, Beijing 100191, China.*

E-mail: zjy@buaa.edu.cn;

[b] *School of physics and Electronic Engineering, Xinxiang University, Xinxiang, 453003, China.*

[c] *Beijing National Research Center for Information Science and Technology, Tsinghua University, Beijing 100084, China.*

E-mail: wangyuyan@tsinghua.edu.cn

Table S1 Lattice constants (Å) of MXs (M = Ge, Sn; X=S, Se, Te) after geometry relaxation.

MXs	Bulk			Monolayer	
	a	b	c	a	b
GeS	4.34	3.67	10.62	4.44	3.64
GeSe	4.45	3.85	10.99	4.27	3.93
GeTe	4.64	4.15	11.53	4.27	4.21
SnS	4.30	4.00	11.34	4.11	4.07
SnSe	4.39	4.19	11.59	4.31	4.25
SnTe	4.72	4.43	12.07	4.51	4.50

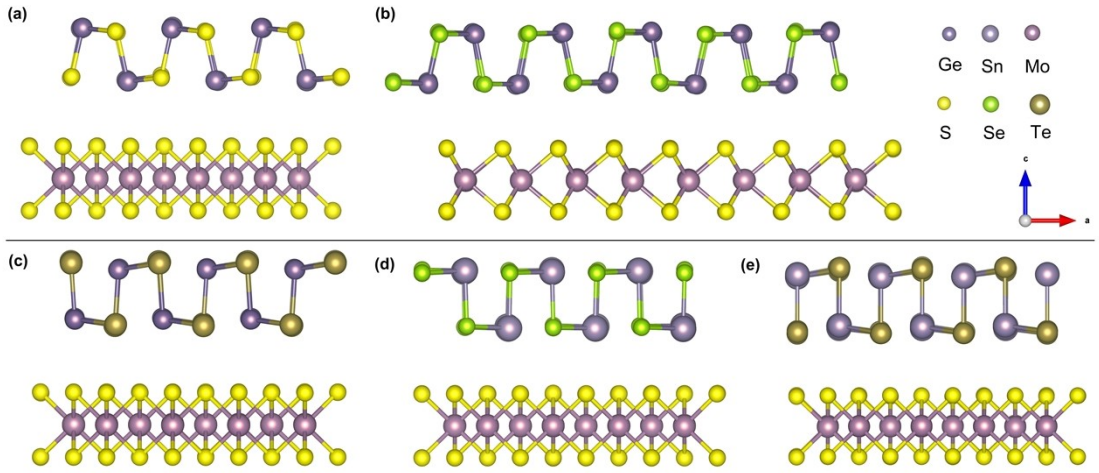

Fig. S1 Side view of (a) GeS/MoS_2, (b) $GeSe/MoS_2$, (c) $GeTe/MoS_2$, (d) $SnSe/MoS_2$, and (e) $SnTe/MoS_2$ heterojunctions.

Part 1. Regulation of interfacial stacking patterns

In order to explore the effect of different stacking of atoms between layers on the system, six high-symmetry stacking patterns are considered by moving MXs in the direction a/b: M atom in MXs is equally positioned with Mo atom (S1), S atom (S2) and middle of Mo-S bond (S3), or two layers are arranged stochastically (S4), the rhombus ring in MXs stacks the middle of hexagonal ring in MoS_2

(S5), the rhombus ring in MXs and hexagonal ring in MoS_2 stacks approximately matching (S6), respectively. The details are illustrated in the circle in Fig.S2. The results show that the effects of different interfacial stacking patterns on the binding energy of the heterojunction are small. The systems with lowest interface binding energy are selected as the most stable MXs/MoS_2 heterojunctions for subsequent research.

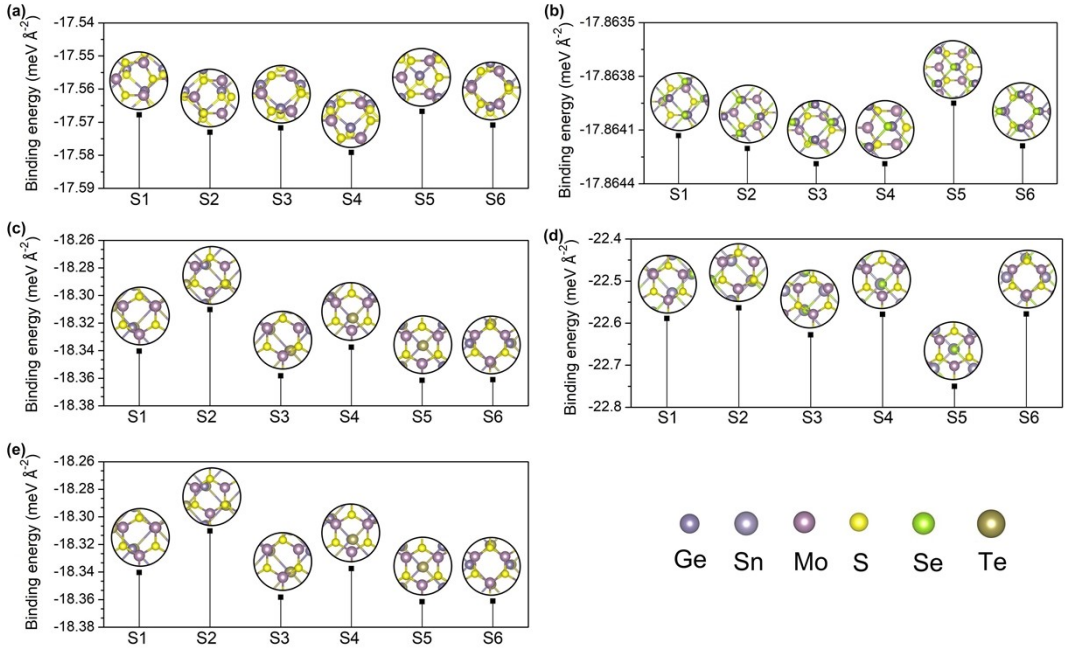

Fig. S2 Binding energies for the six high-symmetry stacking patterns (S1-S6) of (a) GeS/MoS_2, (b) GeSe/MoS_2, (c) GeTe/MoS_2, (d) SnSe/MoS_2, and (e) SnTe/MoS_2 heterojunctions.

Table S2 Detailed structural information of MXs (M = Ge, Sn; X=S, Se, Te)/MoS_2 vdW heterojunction systems

Systems	Supercell	optimized lattice structural information (Å)	maximum lattice mismatches	interfacial binding energy (meV/ Å²)
GeS/MoS_2	GeS: 3×3 MoS_2: $4 \times 2\sqrt{3}$	a=11.00 b=13.03	a: 1.90 % b: 0.66 %	-17.58 (S4)
GeSe/MoS_2	GeSe: 5×4 MoS_2: $5 \times 4\sqrt{3}$ $(R = 90°)$	a=22.15 b=15.98	a: 3.74 % b: 1.75 %	-17.86 (S4)
GeTe/MoS_2	GeTe: 3×4 MoS_2: $4 \times 3\sqrt{3}$	a=12.79 b=16.61	a: 0.21 % b: 1.25 %	-18.36 (S3)
SnS/MoS_2	SnS: 3×4 MoS_2: $4 \times 3\sqrt{3}$	a=12.79 b=16.61	a: 3.81 % b: 2.03 %	-17.73 (S1)
SnSe/MoS_2	SnSe: 3×4 MoS_2: $4 \times 3\sqrt{3}$	a=12.80 b=16.69	a: 1.06 % b: 2.33 %	-22.61 (S5)
SnTe/MoS_2	SnTe: 3×5 MoS_2: $4 \times 4\sqrt{3}$	a=13.01 b=22.30	a: 2.00 % b: 1.58 %	-21.62 (S5)

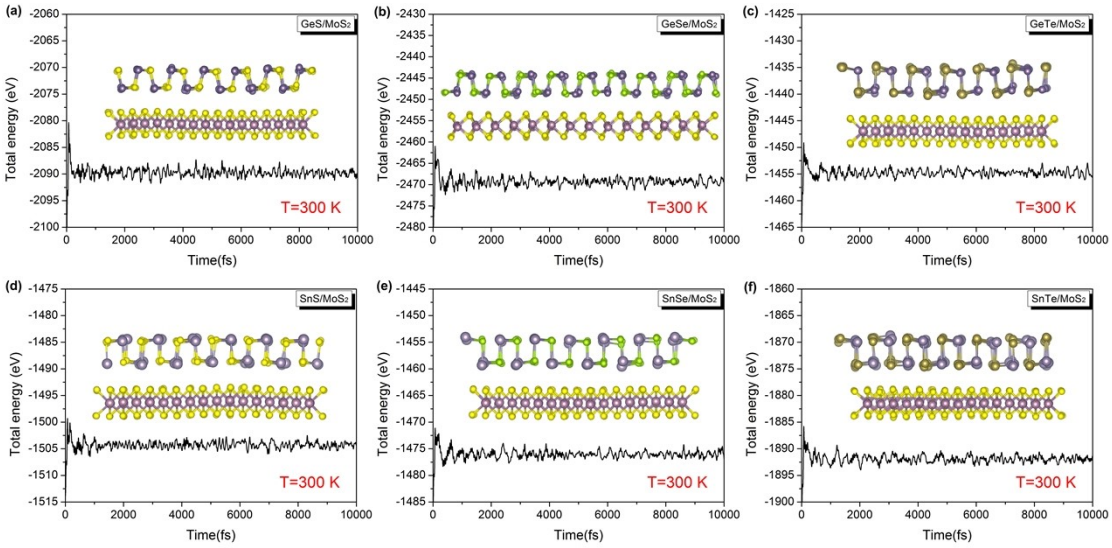

Fig. S3 Total energy fluctuations during AIMD simulations of (a) GeS/MoS_2, (b) $GeSe/MoS_2$, (c) $GeTe/MoS_2$, (d) SnS/MoS_2, (e) $SnSe/MoS_2$, and (f) $SnTe/MoS_2$ heterojunctions. The insets show snapshots of the structures at 300 K at the end of the 10 ps AIMD simulation.

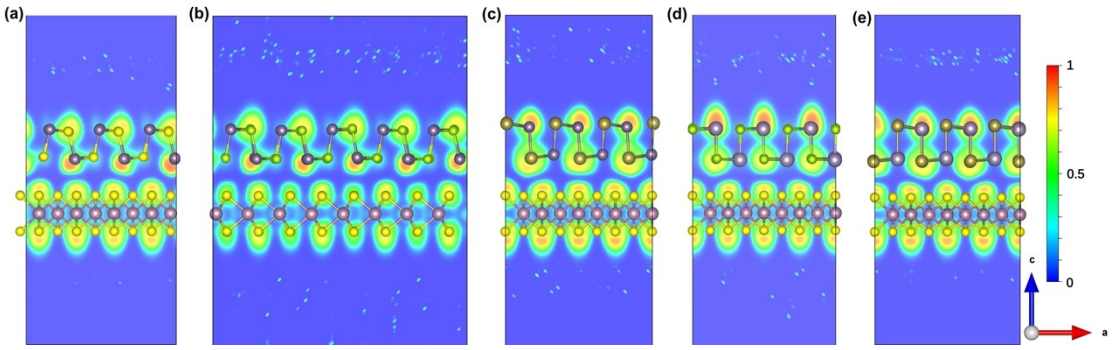

Fig. S4 ELFs of (a) GeS/MoS_2, (b) $GeSe/MoS_2$, (c) $GeTe/MoS_2$, (d) $SnSe/MoS_2$, and (e) $SnTe/MoS_2$ heterojunctions.

Part 2. Interfacial charge-carrier transfer

The plane-integrated electron density difference is defined according to the following equation:

$$\Delta\rho = \rho_{MXs/MoS_2} - \rho_{MXs} - \rho_{MoS_2} \quad (1)$$

where ρ_{MXs/MoS_2}, ρ_{MXs}, and ρ_{MoS_2} are the plane-averaged electron densities of MXs/MoS_2, MXs and MoS_2, respectively. The notable electron rearrangement localizes at the interface and this behavior is visually revealed in Fig. S5. The holes accumulate in the region close to the MXs layer, while the electrons accumulate in the region close to the MoS_2 layer.

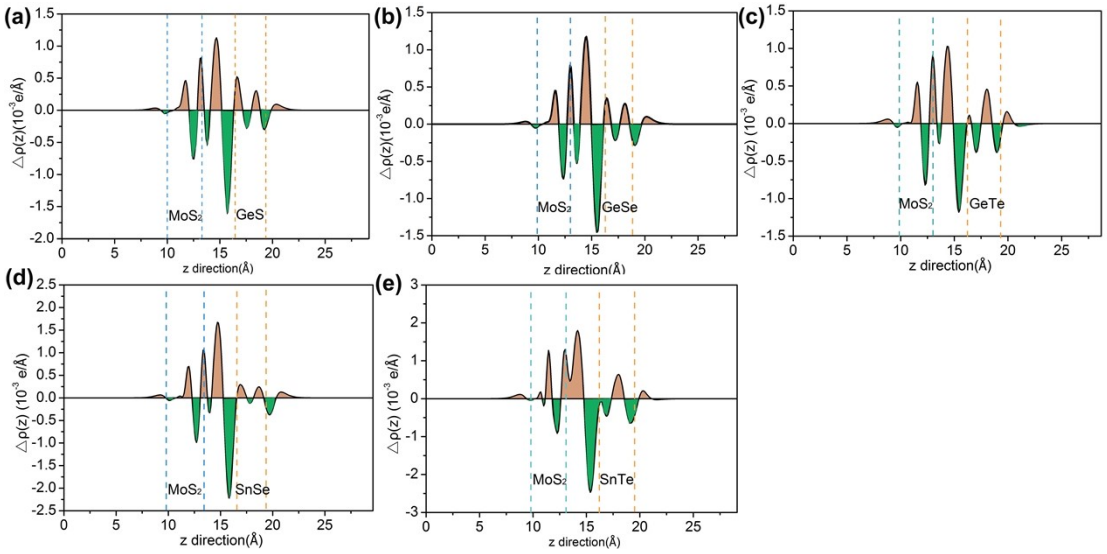

Fig. S5 Plane-integrated electron density differences along *z* direction for (a) GeS/MoS_2, (b) GeSe/MoS_2, (c) GeTe/MoS_2, (d) SnSe/MoS_2, and (e) SnTe/MoS_2 heterojunctions. The dusty pink and green regions represent electron accumulation and depletion, respectively.

Part 3. Electronic structures of MXs/MoS_2

To evaluate the potential of MXs/MoS_2 (M=Ge, Sn; X=S, Se, Te) vdW heterojunction as direct Z-scheme heterojunction, we investigate the electronic structure of MXs/MoS_2 vdW heterojunctions by PBE function (Fig. S6). The valence band is mainly contributed by nonmetal element X (X=S, Se, Te), and the conduction band is mainly contributed by metal element M (M=Ge, Sn). The band structures of GeS/MoS_2, GeSe/MoS_2 and SnS/MoS_2 heterojunctions are shown in Figs. S 6a, b, and d. The density of states (DOSs) show that the valence band maximum (VBM) of GeS (GeSe or SnS) is lower than that of MoS_2, while the conduction band minimum (CBM) is higher than MoS_2. A typical Type-Ⅱ alignment forms because of the apparent band gap caused by their interlaced VBM and CBM. However, the energy levels of GeTe/MoS_2, SnSe/MoS_2 and SnTe/MoS_2 are approximately continuous and do not constitute Type-Ⅱ alignment (Figs. S6c,e,and f), due to the apparent overlap of energy ranges between the VBM and the bottom of CBM. This is mainly due to the filling of Se and Te atoms with more extranuclear electrons than S, leading to the VBM moving to the direction of high energy. Moreover, Sn has more extranuclear electrons, which widens the energy level hybridization and moves the CBM downward.

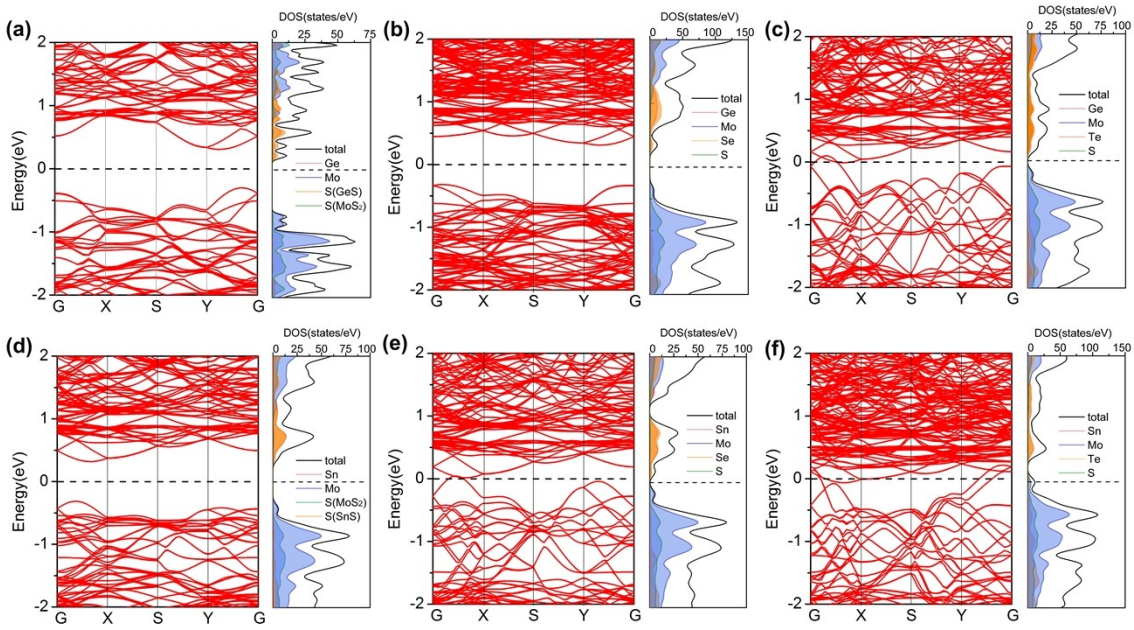

Fig. S6 Band structures and DOSs of (a) GeS/MoS_2, (b) GeSe/MoS_2, (c) GeTe/MoS_2, (d) SnS/MoS_2, (e) SnSe/MoS_2, and (f) SnTe/MoS_2 heterojunctions calculated using PBE function. The orange and blue projective insets areas in DOSs represent the quantum states of MXs and MoS_2, respectively.

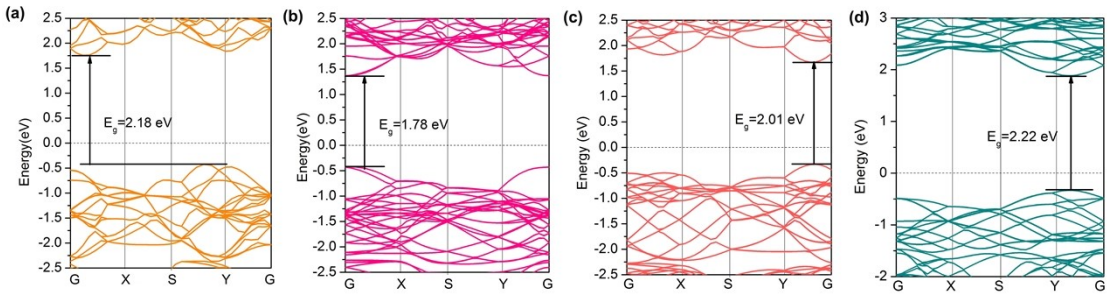

Fig. S7 Band structures of isolated (a) GeS, (b) GeSe, (c) SnS, and (d) MoS_2 monolayers calculated using HSE06.

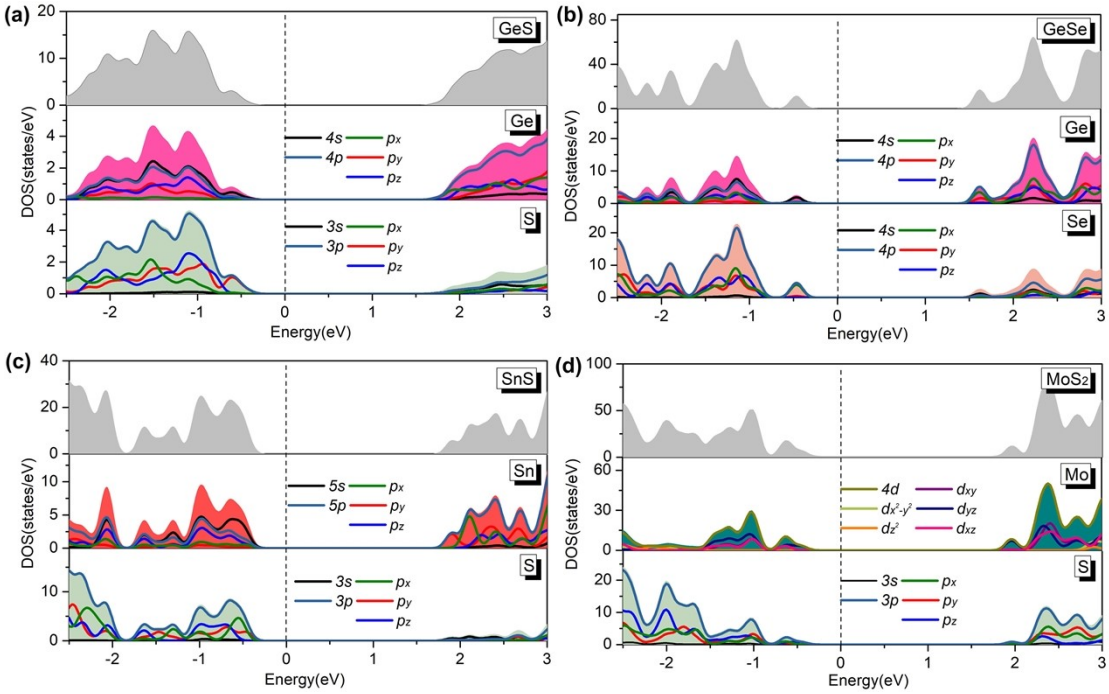

Fig. S8 Total and partial DOSs of isolated (a) GeS, (b) GeSe, (c) SnS, and (d) MoS_2 monolayers calculated using HSE06.

Table S3 Band gaps (eV) before (Eg_1) and after forming heterojunction (Eg_2), and the corresponding potential of VBM and CBM vs. vacuum energy level.

System	isolated layer			MXs/MoS_2 heterojunction		
	Eg_1	VBM_1	CBM_1	Eg_2	VBM_2	CBM_2
GeS	2.18	-5.25	-3.07	2.04	-5.42	-3.38
GeSe	1.78	-5.03	-3.25	1.74	-5.14	-3.40
SnS	2.01	-5.06	-3.05	1.99	-5.15	-3.16
MoS_2	2.22	-6.11	-3.89	--	--	--
MoS_2 (in GeS/MoS_2)	--	--	--	1.85	-6.40	-4.55
MoS_2 (in GeSe/MoS_2)	--	--	--	1.91	-6.23	-4.32
MoS_2 (in SnS/MoS_2)	--	--	--	1.88	-6.24	-4.36

Part 4. Work function

The work function (Φ) is calculated using the following equation [S1]:

$$\Phi = E_{vac} - E_f \quad (2)$$

where E_{vac} represents the energy level of a stationary electron in the vacuum, which is nearby the material surface. E_F represents the Fermi level of the corresponding materials.

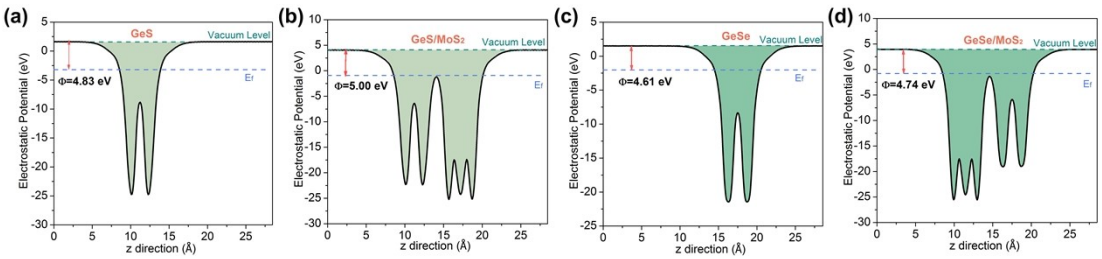

Fig. S9 Electrostatic potentials of (a) GeS monolayer, (b) GeS/MoS_2 heterojunction, (c) GeSe monolayer and (d) GeSe/MoS_2 heterojunction. The green and blue dashed lines represent the vacuum and Fermi levels, respectively.

Table S4 Formation energy of vacancy (eV) in GeS, GeSe, SnS and MoS_2

System	GeS/MoS_2	GeSe/MoS_2	SnS/MoS_2
V_{Ge}	1.97	1.64	--
V_{Sn}	--	--	1.67
V_S	2.14	--	2.04
V_{Se}	--	2.29	--
V_S on MoS_2 surface	2.94	2.81	2.83

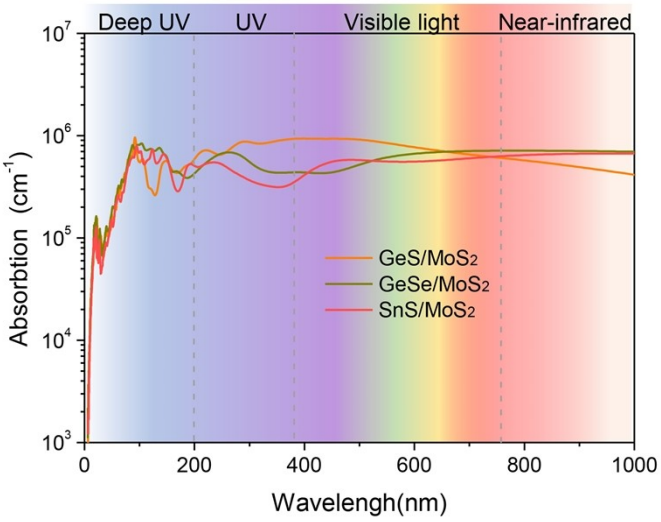

Fig. S10 Absorption spectra of GeS/MoS_2, GeSe/MoS_2, and SnS/MoS_2 heterojunctions by HSE06 method.

Part 5. The absorption spectra of distorted GeS (GeSe or SnS) and MoS_2

The direct Z-scheme requires the photoexcitation to proceed on the two monolayers separately. [S2] To reflect the photoelectron transition mechanism of two-step excitation in Fig. 5b. The absorption spectra of distorted GeS (GeSe or SnS) and MoS_2 monolayers are calculated separately to reflect the optical absorption of the heterojunction. Notably, distorted instead of pristine monolayer GeS (GeSe or SnS) and MoS_2 are used for the optical absorption calculation. In the heterojunctions, the geometrical configurations of the GeS (GeSe or SnS) and MoS_2 monolayers are distorted by interfacial vdW, in contrast to the pristine monolayers. In order to accurately reflect the absorption of the heterojunction by calculating the absorption spectrum of each layer,

we used the crystal structure of the distorted GeS (GeSe or SnS) and MoS_2 single layers, which were separated from GeS/MoS_2, GeSe/MoS_2, and SnS/MoS_2 heterojunction crystal structures after geometry optimization, respectively. Then, the optical properties of the as-obtained crystal structure are calculated by HSE06 to characterize the optical absorption of heterojunctions, as shown in Fig. 6. This is also an accepted means for DFT to characterize heterojunction absorption spectra, as reported previously. [S3,S4]

Part 6. Activity of OER for SnS/MoS_2 heterojunctions surface

The OER for SnS/MoS2 heterojunction on MoS_2 surface is studied. On MoS_2 surface of the SnS/MoS_2 heterojunction, H_2O, *OH, *O, and *OOH are considered. Based on the lower formation energy (Table S4), SnS/MoS_2 with S vacancy on MoS_2 surface is constructed for comparison. For intrinsic heterojunction, surface S atom is considered as active site. For the system containing S vacancy, two kinds of active sites are considered, including Mo suspension caused by S atom deletion and S atom which is the nearest neighbor to S vacancy. The ΔG of OER is calculated in Fig. S11. Surface S atoms in pristine SnS/MoS_2 heterojunction do not have an advantage in OER reaction, because when U=1.23 V (the theoretical lowest value of OER reaction voltage), an overpotential of about 2.46 eV is obtained, which means a considerable barrier to overcome (Fig. S11a). For the system with S vacancy on the surface, the next-nearest-neighboring S atom does not lower the barrier (Fig. S11b). The Mo suspension caused by the loss of S atom has a too strong adsorption capacity for intermediate species *OH, *O. However, when *OOH is adsorbed, three neighboring Mo suspensions compete with each other and totally break the O-O bond in *OOH (Fig. S11c). The reason for the *OOH dissociation is that the strong electronegativity difference between Mo suspensions and O atom break the O-O covalent bond in *OOH intermediates. In conclusion, the surface of pristine MoS_2, whether or not it contains S vacancies, does not provide active sites for OER. Therefore, the catalytic OER activity of pristine MoS_2 is limited by the inert plane, and the activity needs to be further improved.

The feasible morphology modulation is of great significance for improving the catalytic activity of OER. Previous study found that the local change of Mo:S ratio of the precursor influenced the growth dynamics of the MoS_2 crystal, and led to the geometric shape change of MoS_2 between triangle and hexagon. The boundary atom arrangement of MoS_2 with different morphologies is also different, and the most common is the end of S or Mo atom as the edge.[S5] In this work, MoS_2 nanobelt with different edges of S and Mo atoms are constructed to explore their activation ability for OER reaction. The optimized most energetically favorable adsorbed intermediates of OER for MoS_2-Mo-edge nanobelt shows that Mo suspension bond causes O-O in intermediate species *OOH to break and dissociate (Fig. S11d). On the contrary, the *OOH dissociation phenomenon does not occur at the S edges of MoS_2, indicating that the S edges can be used as the active sites for OER reaction. As shown in Fig. S11e, when U=1.23 V, its overpotential is only 1.13 eV. This is also consistent with the report that MoS_2 quantum dots with abundant boundary can achieve efficient OER activation. [S6]

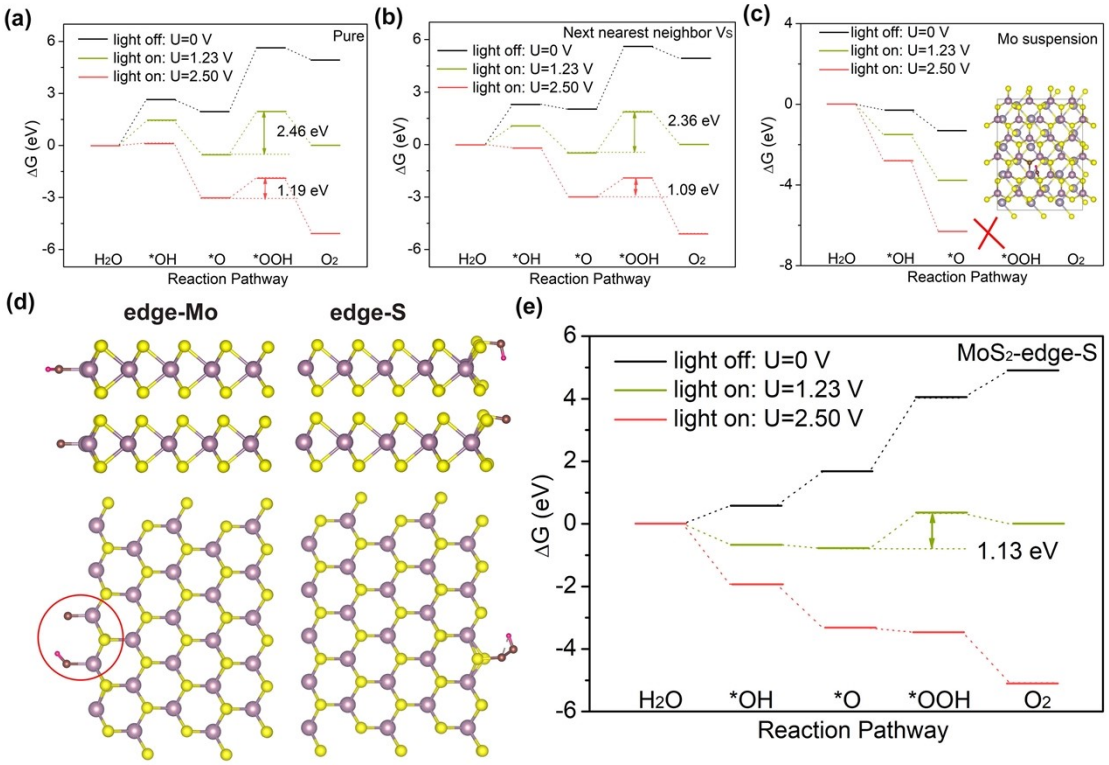

Fig. S11 Calculated ΔG of the OER of SnS/MoS_2 heterojunction on (a) pure MoS_2 surface, (b) S atom next-nearest-neighboring S vacancy and (c) Mo suspension caused by S atom deletion. (d) Optimized most energetically favorable adsorbed intermediates (OH*, O*, OOH*) of MoS_2 nanobelt models. (e) Calculated ΔG of the OER of MoS_2 edge-S.

References

S1 C. X. Xia, J. Du, X. W. Huang, W. B. Xiao, W. Q. Xiong, T. X. Wang, Z. M. Wei, Y. Jia, J. J. Shi and J. B. Li. *Phys Rev B,* 2018, **97**, 115416.

S2 Z. Wang, C. Li and K. Domen. *Chem. Soc. Rev.*, 2019, **48**, 2109.

S3 Q. Yin, C. Yang, M. Wang and X. Ma. *J. Mater. Chem. C*, 2021, **9**, 12231.

S4 L. Ju, Y. Dai, Wei Wei, M. Li and B. Huang. *Appl. Surf. Sci.*, 2018, **434**, 365–374.

S5 S. Wang, Y. Rong, Y. Fan, M. Pacios, H. Bhaskaran, K. He and J.H. Warner. *Chemistry of Materials,* 2014, **26**, 6371-6379.

S6 B. Mohanty, M. Ghorbani-Asl, S. Kretschmer, A. Ghosh, P. Guha, S. K. Panda, B. Jena, A. V. Krasheninnikov and B. K. Jena. *ACS Catal.,* 2018, **8**, 1683-1689.